Development and Characterization of An Unshielded PatLoc Gradient Coil for Human Head Imaging

ANNA WELZ,[1] CHRIS COCOSCO,[1] ANDREW DEWDNEY,[2] DANIEL GALLICHAN,[3] FENG JIA,[1] HEINRICH LEHR,[4] ZHENYU LIU,[5] HANS POST,[4] HARTMUT SCHMIDT,[4] GERRIT SCHULTZ,[1] FREDERIK TESTUD,[1] HANS WEBER,[1] WALTER WITSCHEY,[6] JAN KORVINK,[7,8] JÜRGEN HENNIG,[1] MAXIM ZAITSEV[1]

[1] *Department of Diagnostic Radiology, Medical Physics, University Medical Centre Freiburg, Freiburg, Germany*
[2] *Healthcare Sector, Siemens AG, Erlangen, Germany*
[3] *CIBM, EPFL, Lausanne, Switzerland*
[4] *Bruker BioSpin MRI GmbH, Ettlingen, Germany*
[5] *State Key Laboratory of Applied Optics, Changchun Institute of Optics, Fine Mechanics and Physics (CIOMP), Chinese Academy of Sciences, Changchun, China*
[6] *Department of Radiology, University of Pennsylvania, Philadelphia, PA, USA*
[7] *Department of Microsystems Engineering—IMTEK, University of Freiburg, Freiburg, Germany*
[8] *Freiburg Institute of Advanced Studies—FRIAS, University of Freiburg, Freiburg, Germany*

Abstract: A cylindrical head gradient insert for human imaging with non-linear spatial encoding magnetic fields (SEMs) has been designed, optimized and successfully integrated with a modified 3T clinical MR system. This PatLoc (parallel acquisition technique using localized gradients) SEM coil uses SEMs that resemble second-order magnetic shim fields, but with much higher amplitude as well as the possibility for rapid switching. This work describes the optimization of a coil design and measurement methods to characterize its SEMs, induced self-eddy currents and concomitant fields. Magnetic field maps of the SEMs are measured and it is demonstrated that the induced self-eddy current magnetic fields are small and can be compensated. A method to measure concomitant fields is presented and those fields are compared to simulated data. Finally, in vivo human images acquired using the PatLoc system are presented and discussed. © 2013 Wiley Periodicals, Inc. Concepts Magn Reson Part B (Magn Reson Engineering) 43B: 111–125, 2013

INTRODUCTION

Magnetic resonance imaging with non-linear SEMs has been proposed (*1*) and demonstrated (*2*). The

concept of parallel acquisition technique using localized SEMs (PatLoc) has the potential for reduced image acquisition and increased spatiotemporal resolution by exploiting the faster switching rates possible with localized encoding fields.

This was demonstrated with PatLoc only acquisitions using the linear *z*-gradient for slice selection and two non-linear PatLoc spatial encoding magnetic fields (SEMs) for in plane encoding (*2*) and was also applied to a radial sequence (*3*). Acceleration using parallel imaging techniques with reduced number of acquired *k*-space lines with higher acceleration factors was also successfully demonstrated

(4). All these experiments, on phantoms and volunteers, had improved image resolution at the periphery but reduced resolution in the middle of the acquired images due to the characteristics of the SEMs (1–3). To overcome this limitation, PatLoc and linear SEMs are combined with the 4D-RIO (5) or North West EPI (6) acquisition techniques. Further applications of the PatLoc SEMs include GradLoc (7), where the PatLoc SEMs are used for phase preparation to allow for imaging with the linear SEMs with reduced field-of-view (FOV) without folding artefacts. Slice selection using the PatLoc SEMs has also been successfully applied to imaging of curved slices, adapted to the anatomy of the human head (8).

However, imaging with non-linear SEMs can be challenging due to gradient system imperfections. These problems are exacerbated when linear and non-linear SEMs are driven simultaneously and with high amplitudes (3,6,9,10). Special consideration needs to be given for undesired magnetic fields such as the so-called concomitant fields produced together with the primary magnetic field (11), and eddy current fields, magnetic fields resulting from induced currents in the SEM coil conducting elements (12).

The effects of concomitant magnetic fields and eddy currents are important because of their potential dephasing effects and artefacts in images as in single shot acquisitions, e.g., with 4D-RIO (5) or North West EPI (6). To account for the concomitant fields, it is important to consider the transverse components B_x and B_y of the full magnetic field vector field **B** produced by the spatial encoding magnetic fields (SEMs) and not only the z-component B_z (13). Full characterization of the electromagnetic properties of a SEM coil includes the measurement of B_z fieldmaps, measurement and evaluation of the fields from eddy currents and characterization of B_x and B_y, the transverse components which lead to the concomitant fields. Coil performance was characterized based on simulations as well as by experiments. The MR-relevant field components B_z and $B_t = \sqrt{\left(B_x^2 + B_y^2\right)}$ were measured directly by MRI. Comparison of experimental data of B_z and B_t with simulation was used to verify the field simulations. The full B vector field from the simulations was used for the assessment of peripheral nerve stimulation (PNS) (14) estimation, an important safety consideration, and a necessary step for obtaining IRB approval (15) for human imaging.

This article describes the design and manufacture of the first in-house built PatLoc SEMs coil using non-linear spatial encoding magnetic fields for human head imaging (16). Design constraints such as available space within the scanner bore and practical realization are discussed; the final layout and electrical properties are also presented. A electromagnetic characterization is presented including a spherical harmonics analysis of the 3D SEM. MR sequences were developed to measure eddy currents and B_t. Compensation of the measured eddy currents allows better performance of the PatLoc SEM coil reducing unwanted dephasing artefacts. Measured concomitant fields were compared to simulated field data to confirm the validity of the magnetic field simulation which was used for PNS predictions for human *in vivo* imaging. Finally, human *in vivo* images were obtained.

MATERIALS

To realise proof-of-principle *in vivo* PatLoc experiments a PatLoc SEM coil was built to operate with a 3T system (MAGNETOM Trio, a Tim system, Siemens Healthcare, Erlangen, Germany). This setup imposes geometric restrictions such as the scanner bore opening (600 mm) and the decision to design the PatLoc SEM coil to rest on the patient
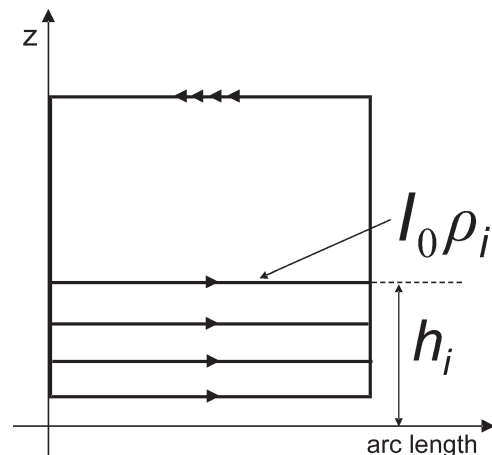
Figure 1 The design variables and the basic layout of a single SEM coil element, including the current I_0, the direction of the current ρ_i and the position of the wire elements along the z-direction h_i.

---

table rails. This leads to an outer diameter of 520 mm for this PatLoc SEM coil. Being dedicated to human head imaging, the isocenter of the PatLoc SEM coil was set to 165 mm from the patient end of the PatLoc SEM coil (Fig. 2)—assuming this would comfortably reach approximately the center of the brain in most subjects, with the shoulders outside of the coil (17).

Four coil elements were used to generate each of the two quadrupolar PatLoc SEMs (A22 and B22 in spherical harmonics), resulting in the total of eight elements arranged on two cylindrical layers mounted upon a glass–fiber reinforced plastic (GRP) cylindrical former with 355 mm inner and 385 mm outer diameter and 1,000 mm length. The individual PatLoc SEM coil elements were of rectangular shape for easier manufacturing, with the maximum arc length constrained to 300 mm and the maximum length to 700 mm. The maximum intended driving current for this PatLoc SEM coil was 100 A. With these constraints and the multipolar SEMs as the target fields, the optimization of the PatLoc SEM coil elements was performed as described in the next section (also cf. (18)).

Design of the Coil Elements

For optimization of the coil layout based on the basic layout described above the ground structure approach (GSA) (19) was used. Based on an assumed (user-specified) initial coil layout (see Fig. 1), the GSA was used to determine whether there is a conductor or not for all possible wire positions. The design purpose of an optimized coil is to generate the required magnetic field distribution in the region of interest (ROI), which we chose for this PatLoc SEM coil to be a cylinder with $r = 125$ mm and $z \pm 150$ mm around the isocenter with a cylindrical design surface for the coil elements with radius 192.5 mm and 700 mm heights. To obtain the required magnetic field distribution in the ROI, the first objective function was chosen as:

$$\phi_1 = \int_{\text{ROI}} \sum_{i=1}^{n} \left(B_z(I_0, \rho_i, h_i) - B_z^* \right)^2 \, d\Omega \qquad (1)$$

where B_z is the calculated magnetic field, and which was obtained by the Biot-Savart law and B_z^* the target magnetic field, I_0 is the current passing through the conductors, ρ_i the design variable which expresses whether the conductors exist or not, and h_i is the design variable which locates the positions of the conductors as shown in Fig. 1. This figure depicts an early stage of the iterative optimization

with a simplified model of the PatLoc SEM coil elements. This figure depicts an early stage of the iterative optimization with a simplified model of the PatLoc SEM coil elements. The GSA optimized the number of windings and the positions of the rungs generating the target field (colored red in Fig. 4), but included the entire PatLoc SEM coil element in the simulations during the optimization process. B_z^* is the z-component of a target magnetic field and n is the number of the ground structure conductors.

To obtain discrete conductors at the final stage of optimization, the second objective function was chosen as:

$$\phi_2 = \sum_{i=1}^{n} \left[\rho_i (1 - \rho_i)(1 + \rho_i) \right]^2 \qquad (2)$$

where ρ_i is in the interval $[-1,1]$. The form of Eq. (2) was chosen such that minimization of ϕ_2 penalizes intermediate values of ρ_i toward the integers $\{-1,0,1\}$. Values of -1 or $+1$ are interpreted as current flowing in one or the other direction, whereas a value of zero corresponds to no current and therefore no wire.

To design a manufacturable PatLoc SEM coil, a fabrication constraint for the wire thickness

$$|h_k - h_j| \geq \delta \qquad j, k = 1, \ldots, n; \; j \neq k \qquad (3)$$

was added in the optimization problem (Fig. 1). The weighted sum approach was used to transform the multi-objective optimization problem into a single-objective optimization problem, i.e., the weighted sum $\phi_\omega = \omega_1 \phi_1 + \omega_2 \phi_2$ of the two objectives ϕ_1 and ϕ_2 was used with the design variables h_i being the position along the z-direction and ρ_i being the direction of the current including the constraint for the wire thickness, see Eqs. (1–3). The weights were set to be $\omega_1 = 0.91$ and $\omega_2 = 0.09$. The optimization software SNOPT in Comsol 3.5 (Comsol optimization lab, Stockholm, Sweden) was used to solve the single-objective optimization problem with inequality constraints. This solver is deterministic and the optimization finds a local optimum for this specific problem.

Based on an initial conductor distribution, the conductors were grouped manually into rungs with a minimum of three and a maximum of five conductors per rung for better mechanical stability of the PatLoc SEM coil before optimising the final position of the rungs. The return paths were grouped and placed as far as possible from the isocenter to minimize effects on the target magnetic field. The optimization method is described in more detail in (20).
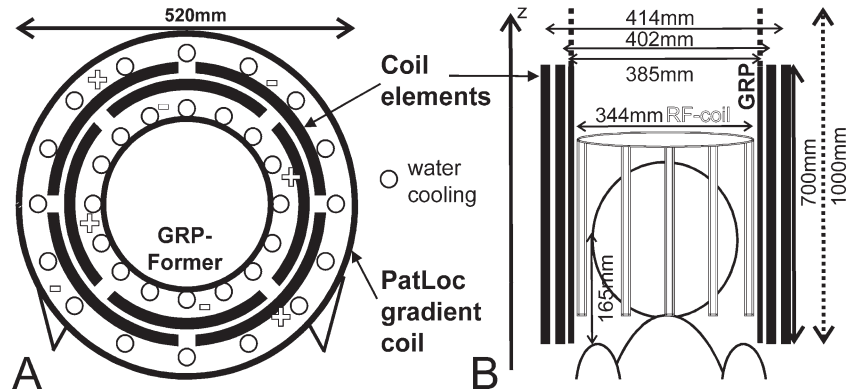
Figure 2 Cross section and longitudinal drawing of the PatLoc SEM coil (not to scale—dimensions marked). (A) The GRP-former, the water cooling and two layers of coil elements amounting to the final outer diameter of 520 mm are schematically drawn. The ± signs indicate the current flowing in the individual coil elements, to generate PatLoc SEMs. (B) A longitudinal drawing including the diameters of the two PatLoc layers and the insert RF-coil. The distance from the isocenter to the edge of the insert is 165 mm.

Coil Construction

Eight of these coil elements were wound with 2.7 mm enamel-insulated copper wire by BRUKER (Biospin, Ettlingen, Germany) and shaped to match the radius of the former. Water cooling was implemented using a plastic tube with a diameter of 4 mm (PA 12. OD 4 mm, ID 2.5 mm, from TECA-LEMIT GmbH), provided by Siemens Healthcare. The first layer of water cooling was directly glued to the above mentioned GRP former. To ensure that epoxy flowed into all cavities during the casting process, a spiral design of the water cooling, with 10 parallel circuits per layer, was realised. The circuits were connected so as to ensure opposing flow directions in the adjacent tubes. 1-to-5 brass water connections were used to connect the scanners cooling hoses to the PatLoc SEM coils water cooling tubes. The brass connections are Siemens own construction, with IQSM M54 I: Straight push in fitting M 5–4 mm, mini m. hexagon socket fittings (Landefeld Druckluft und Hydraulik GmbH, Kassel, Germany).

To further ensure the absence of closed cavities, spacers of 7 mm (4 + 3 mm) height were mounted on the GRP former to bear the first layer of PatLoc SEM coil elements. Additional spacers with 3 mm height were placed between the first and second layer of PatLoc SEM coil elements. The second layer of water cooling tubes was mounted directly on the coil elements, see Fig. 2 for a cross sectional representation of the PatLoc SEM coil. The final diameters of the coil layers were 402 mm and 414 mm measured from the center of the wire. Each layer of the PatLoc SEM

coil consists of four individual coil elements (Fig. 2) connected in series. The resistance and inductance were measured using an LCR-meter (HAMEG Instruments GmbH, Mainhausen, Germany). The coil was also tested for electrical insulation (I3304D from SPS-electronic) before casting in low viscosity epoxy resin (Huntsman Advanced Materials GmbH, Bad Säckingen, Germany).

The PatLoc SEM coil rests on rollers which were mounted to the final cast PatLoc SEM coil for easier handling. The rollers were positioned such that the PatLoc SEM coil is rotated by 22.5° to the scanner's coordinate system to reduce coupling of the individual channels of the PatLoc SEM coil from the second order shims which have very similar magnetic fields.

An RF head coil set from Siemens Healthcare (Erlangen, Germany), originally designed for an MRI-PET head insert, with a one-channel transmit-receive coil surrounding an eight channel receive array, with 344 mm outer and 260 mm inner diameter, was tuned and matched for use with the PatLoc SEM coil. The RF shield from a Siemens linear SEM insert coil was fixed onto the inner bore of the PatLoc SEM coil, to provide the correct RF environment for this Tx/Rx head coil.

The completed PatLoc SEM coil was integrated into the modified Siemens Trio MR system with an additional three channel SEM power amplifier (GPA), which can be driven independently from the standard linear SEMs. The scanner was equipped with Siemens TX-Array hardware capable of driving seven additional independent sequence controllers with seven independent transmit RF channels (21).

Each of these sequence controllers is also capable of driving three gradient amplifiers. This hardware setup was used to control one additional GPA through one of the additional sequence controllers of the TX-array, resulting in a total of six gradient channels for this modified scanner. All gradient channels can be driven independently and simultaneously. Only small modifications are then required to existing pulse sequences to add the capability to select which channel is used for frequency and phase encoding.

Transverse Magnetic Field Components and Concomitant Fields

A magnetic field is a vector field, but typically only B_z is considered for signal encoding and image reconstruction. Usually B_x and B_y are small enough so that their effect on MR imaging can be considered negligible. However, if B_x and B_y become stronger the transverse component

$$B_t = \sqrt{B_x^2 + B_y^2} \qquad (4)$$

becomes too strong and will lead to distortions of the acquired image.

Following Bernstein's paper (11), the actual magnetic field used for imaging (B_{img}) at a particular location becomes:

$$B_{img} = \sqrt{(B_0 + B_z)^2 + (B_t)^2}, \qquad (5)$$

so that the local resonance frequency can be written as:

$$\omega = \gamma \ B_{img}. \qquad (6)$$

Further, following (11), with the Taylor series expansion to the second order, the frequency is given by:

$$\tilde{\omega}\gamma\left(B_0 + B_z + \frac{(B_t)^2}{2B_0}\right). \qquad (7)$$

It is important to distinguish between the transverse component of the encoding field B_t (or the corresponding components, B_x and B_y), and the so-called concomitant field, B_c (11). Whereas B_t is a part of a physically existing magnetic field, B_c refers to a virtual field [here with the form ($B_t^2/2B_0$)], introduced to describe the observed phase evolution of the signal.

METHODS

All measured data were acquired on the modified 3T Siemens MR system as described above. For best possible coverage of the entire volume usable for imaging, the eight-channel receive array was removed from this experimental setup for the phantom measurements (with a 240 mm spherical phantom, doped with NaCl and gadolinium), leaving the single-channel transmit/receive coil for these experiments to characterize the PatLoc SEM coil. For all measurements, except for the concomitant field measurements and *in vivo* images, the FOV was $260 \times 260 \ mm^2$ and the slice thickness was 3 mm. The phantom was positioned at the isocenter of the magnet using the service software of the scanner and rested long enough to minimize movement of the fluid in the phantom.

Spatial Encoding Magnetic Fields

For measuring the SEMs [Fig. 3(A)] a standard Gradient Recalled Echo (GRE) Sequence was modified. SEMs were measured through repeating the same sequence twice, once with an extra SEM pulse on one of the PatLoc channels (between each echo of a multi-echo readout) and once without. These extra pulses provoke a phase accumulation due to the PatLoc SEMs, and the measurement without extra pulses was used for correction of the present B_0 inhomogeneities (22,23). Eight echoes were measured to calculate mean SEM fieldmaps.

This extra SEM was a triangular pulse which was driven with 24.9 A for the inner four elements, which we refer to as PatLoc 1, and 26 A for the outer four coil elements, called PatLoc 2, with a duration of 100 μs—from which the sensitivity of the PatLoc SEM coil was calculated. The eight echoes were spaced out by $\Delta TE = 3$ ms. The measurement included 64 slices, each of 3 mm, covering a total volume of $z \pm 90$ mm.

The robust multilinear regression fit routine from Matlab (24) was used to analyse the PatLoc SEMs for their spherical harmonics, following the expression of $B_z(z)$ from Hillenbrand et al. (25), based on Romeo and Hoult (26). The associated Legendre functions were used for the fit as implemented in (27).

The measured data were masked with a binary mask based on the magnitude images of a 200 mm diameter sphere before fitting with spherical harmonics up to the 8th order. The resulting coefficients were used to calculate the magnetic field inside this sphere. The amplitude for each coefficient was normalized to the maximum amplitude of the SEMs and is represented in percentage (%) of the maximum amplitude.
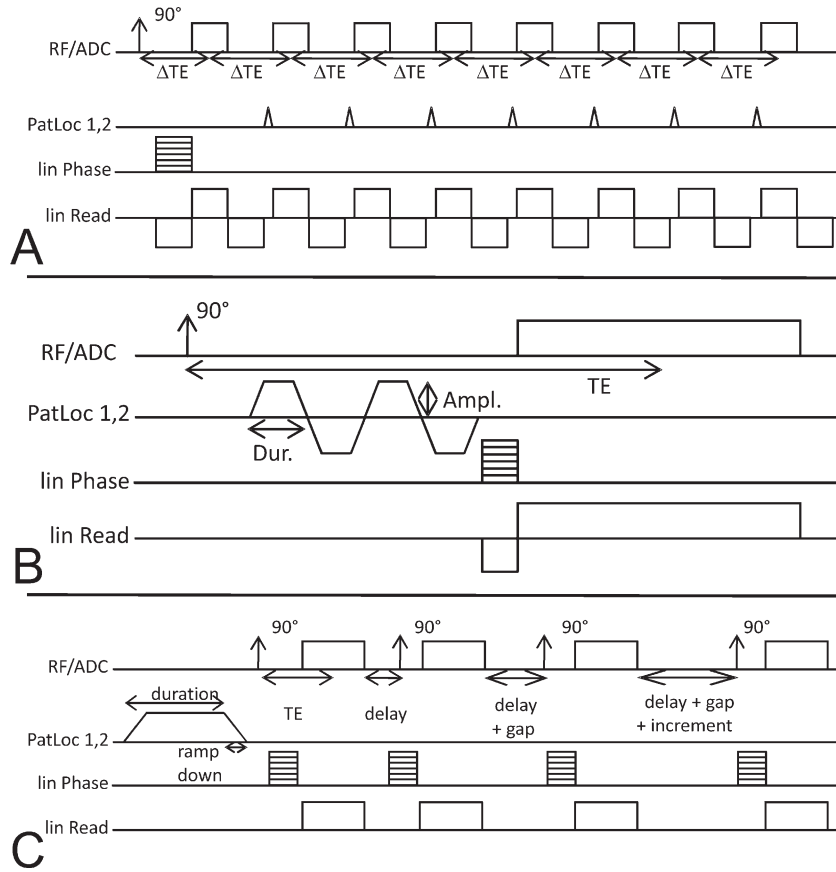
Figure 3 Sketch of the used sequences. (A) The field mapping sequence with eight echoes, of which seven include an extra pulse on the PatLoc SEM coil to generate the fieldmap of a SEM. For reference and B_0 inhomogeneity correction, this is repeated without extra pulses. (B) The sequence to measure the transverse component of the concomitant field. Two sets of extra bipolar SEM pulses were played out on the PatLoc SEM coil, right before the image acquisition. This bipolar SEM refocuses the effect of B_z but will induce a phase due to the concomitant term B_t. (C) The eddy current sequence, where the PatLoc SEM coil is switched with a trapezoidal SEM pulse, which is sufficiently long for decay of the eddy currents induced during ramp-up and resulting eddy currents are attributed to ramp-down only. To measure exponentially decaying eddy currents, the gaps between measurements were increased logarithmically.

Simulated Encoding Fields

A full model of the PatLoc SEM coil was set up in Cobham OPERA 14 3D (Cobham, Oxfordshire, UK) and all magnetic fields were calculated. For easier and faster simulation using symmetry conditions, the model was not rotated to match the orientation of the integrated PatLoc SEM coil.

Transverse Magnetic Fields

To characterise the transverse field component, bipolar SEM pulses were played on one of the PatLoc channels immediately after the slice selection

and before acquiring GRE fieldmaps with the linear gradients. These bipolar SEM pulses reverse the effect of the B_z component of this SEM pulse, hence the phase accumulation due to B_t can be measured (see Eq. (7)).

Two sets of bipolar SEM pulses were used, each individual pulse with a duration of 3 ms, and the maximum possible amplitude of 130 mT/m^2 (amplitude obtained from the calibrated data of the fieldmap measurement [Fig. 3(B)]. This measurement was repeated with inverted SEM pulses to suppress the influence of the eddy currents on the measured B_t maps. Because all return paths of the PatLoc SEM coil were positioned close to the service end

of the PatLoc SEM coil, the concomitant fields have a strong spatial dependency on z. Therefore, a coronal slice in a cylindrical phantom with 170 mm diameter was measured covering approximately 200 mm along the z-direction. The FOV was chosen to be 440 × 208 mm with 2 mm slice thickness and a resolution of 220 × 104 pixels. As the simulated data has the same orientation as the spherical harmonic coefficients A22 and B22, the measured coronal slice was tilted by 22.5° toward the sagittal orientation to compensate for the physical rotation of the actual PatLoc SEM coil.

The simulated data (B_x, B_y, and B_z) were fitted with spherical harmonics in the same way as the measured 3D SEMs, and also B_t was compared with simulated data for validation.

Eddy Currents

For further characterization of the PatLoc SEM coil, magnetic fieldmaps of the induced eddy currents were measured at the magnet isocenter with the linear SEMs using a modified GRE pulse sequence. This sequence includes an extra SEM pulse switched on each PatLoc channel with the amplitude of 17 mT/m^2, the duration of 3,000 ms and a ramp down of 100 μs prior to the fieldmapping sequence using the linear gradients [Fig. 3(C)]. Thirty-two time points were acquired with logarithmic spacing between 5 ms and 3,000 ms, with a TE of 4.8 ms. This was repeated twice for each phase encoding step of the 128 × 128 matrix, once with a negative SEM pulse for the PatLoc SEM, and once without the extra SEM pulse for correction of the background B_0 magnetic field, resulting in a total acquisition time of 50 min.

The fieldmap data from the eddy current measurements were analyzed at each time point for the amplitude of the spherical harmonics up to second order. The results were normalized as a percentage of what the eddy current amplitude would have been if the entire SEM pulse had been fully converted into eddy currents and as if they had persisted for an infinitely long time. A single exponential was fitted to determine the main decay component of the eddy currents. The obtained amplitude and decay times were used as compensation values at the scanner to correct for eddy current effects. This measurement and analysis was repeated with these compensation values to demonstrate the correction. For the compensation, the exponential values were fed into an identical set of gradient controlling DSPs as used for the linear gradients. The method for compensating the PatLoc eddy

currents therefore used the same Siemens Healthcare proprietary firmware as the linear gradients.

Human In Vivo Images

Simulated data from Cobham Opera 3D for the complete vector fields of the PatLoc SEM coil were used to evaluate its safe usage regarding PNS. The simulated data were verified by the above described experimental measurement of the spatial encoding and transverse magnetic fields. A local change of magnetic field of 20 T/s imaging is considered safe by the International Electrotechnical Commission (IEC) within the so-called "normal operation mode." In the initial step, the upper limit of the PatLoc SEM slew rate in the used imaging sequence was determined such that the limit of 20 T/s was not exceeded anywhere in the region accessible by the volunteer (28). If the imaging or contrast parameters required higher slew rates the following procedure has been applied: (1) amplitudes of all the SEMs were scaled down to ensure the 20T/s slew rate limit for PatLoc SEMs is not exceeded; (2) the amplitudes of the SEMs were iteratively increased by no more than 10% per step toward the desired values, while the volunteer's comfort was continuously monitored (29). The above rationale was used to demonstrate the safe usage of the coil to the local ethics committee (15) and became a part of the IRB-approved measurement protocol.

Turbo Spin Echo (TSE) in vivo images of a volunteer were acquired with the following parameters for the linear reference image: FOV 220 × 220 mm^2, TE 8.6 ms and a matrix size of 256 × 252, reconstructed to a 768 × 768 matrix to match the PatLoc reconstruction. The PatLoc image was acquired with TE 8.5 ms, all other parameters were the same for comparable conditions and image contrast. For the PatLoc acquisition, the sequence was modified to use the linear z-gradient for slice selection and the two PatLoc SEMs for 2D in plane encoding. The PatLoc image was reconstructed into a 768 × 768 matrix using a conjugate gradient (CG) (9,10) method.

RESULTS

Optimization and General Electrical Results

The final optimized coil element (16) consisted of 35 windings of 2.7 mm diameter insulated copper wire; it was 700 mm long and has an arc length of 290 mm to allow for sufficient space between the final mounted coil elements, as shown in Fig. 4. The final
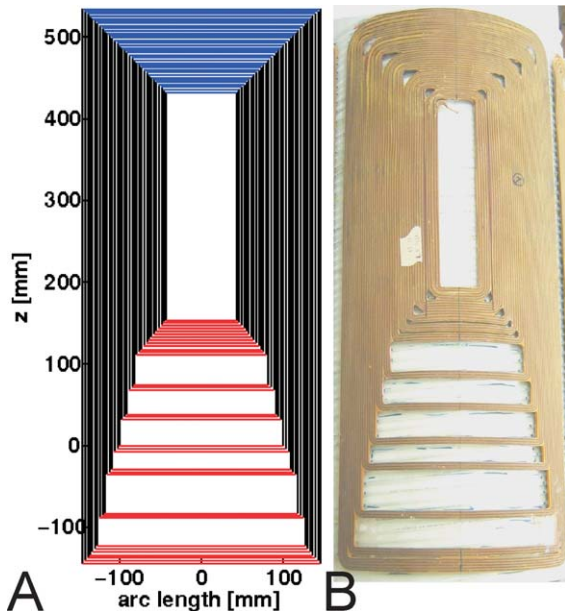
Figure 4 (A) Optimized individual SEM coil element design. The lines in red show the target magnetic field generating rungs, where the positions of the rungs were optimized along the *z*-direction. Blue is used for the densely packed return path. The position at $z = 0$ mm indicates the position of the isocenter of the magnet and the PatLoc SEM coil. (B) Prototype PatLoc SEM coil element based on the optimized coil layout.

length of the wire was 45.63 m, and the resistance was measured as 127 ± 1 mΩ for the individual coil elements. The maximum error in the field over the ROI was 23%, where these errors occur at positions close to the wires. However, the maximum elliptical region which fits into the ROI yielded only 6% deviation from the desired target magnetic field (*29*). The optimization took 220 minutes on a standard desktop

computer. Eight identical coil elements were built where four of these coil elements were connected in series, representing one SEM, resulting in an inductance of 2200 ± 10 µH and a resistance of 510 ± 10 mΩ compared with a linear head gradient insert with an inductance less than 1,000 µH and a resistance less than 400 mΩ.

Before casting in epoxy resin, the PatLoc SEM coil passed high voltage tests up to 4 kV between each of the coil elements ensuring proper electrical insulation. During the casting process approximately 88l of epoxy was used, adding to a total weight of approximately 150 kg for the complete insert. The PID values for the gradient controllers were optimised to prevent voltage overshoots or current oscillations on the corners of trapezoidal pulses using a Siemens Healthcare proprietary service adjustment program, thus matching the amplifiers to the loads and saving the correct values to the amplifier controller firmware. The maximum slew rate of 400 A/ms was determined by comparing the required current signal with the actual output current as measured by the GPA current feedback loop. At the maximum allowed current by the PatLoc SEM coil, the maximum slew rate was defined to be a deviation of more than 2.5% in the rise time, without the onset of "ringing" which could lead to component damage.

Measured Spatial Encoding Magnetic Fields

The inner four coil windings (the field of which we refer to as "PatLoc 1") produce a stronger field than the outer windings ("PatLoc 2" respectively) for the same current, due to the smaller diameter of the windings, see Fig. 5. Also, see Table 1 for detailed
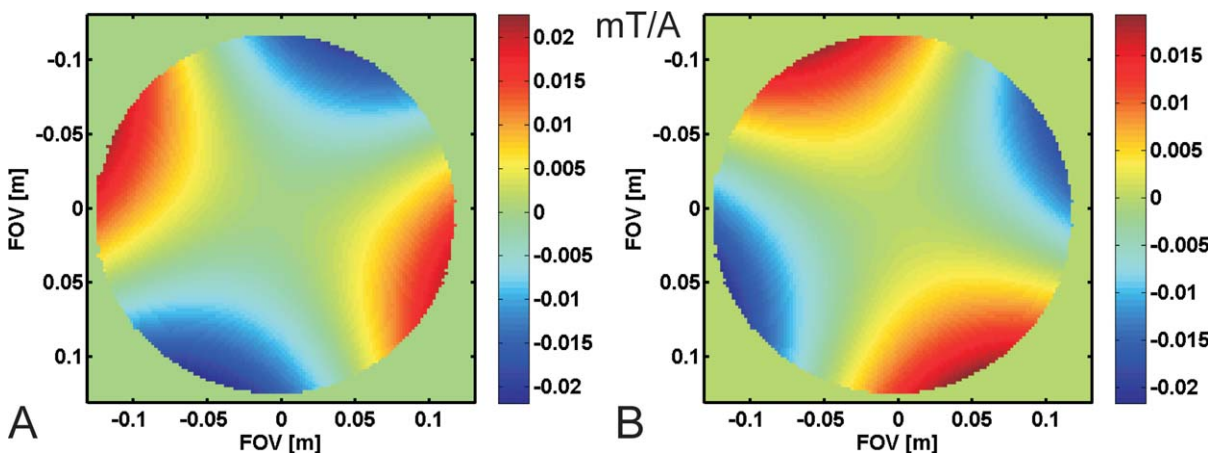
Figure 5 Fieldmaps in mT/A of the PatLoc SEMs. PatLoc 1 (A) and PatLoc 2 (B) For a given current, PatLoc 1 yields slightly higher fields compared with the slightly larger PatLoc 2.

Table 1 The Most Relevant Spherical Harmonic Constituents in % of the Maximum Field Inside the Analyzed Sphere of the Measured Quadrupolar PatLoc Fields

Spherical Harmonic	Analytical Expression	PatLoc 1 %	Combined Amplitude	PatLoc 2 %	Combined Amplitude
A 10	Z	1.16 ± 0.08		0.51 ± 0.08	
A 11	X	2.2 ± 0.8		2.9 ± 0.9	
B 11	Y	3.6 ± 0.9	**4.22**	2.5 ± 0.9	**3.84**
A 22	$X^2 - Y^2$	71.4 ± 9.0		65.3 ± 9.0	
B 22	$2XY$	65.9 ± 9.0	**97.19**	71.7 ± 9.0	**96.93**
A20	$Z^2 - (X^2+Y^2)/2$	0.04 ± 0.9		0.06 ± 0.9	
Rotation angle		$-21°$		$+24°$	
Sensitivity mT/m^2/A		1.44		1.36	

In addition, the O-space A20 Field Is Included.

amplitudes of the fitted spherical harmonics components. The dominant fitted component of the fields was clearly the second order harmonic (A22 and B22), as designed with amplitudes of over 96% and maximum errors of 10%. Additional residual linear terms A10(z), A11(x), and B11(y) were also observed. All other higher order contributions are below 1% and are disregarded. The A20 field (the quadratic field used in another form of non-linear encoding referred to as O-space imaging (*30*)) is also included in the table, but is negligible for the PatLoc SEM coil.

The combined amplitudes add up to over 100% since the algebraic sign of the individual field components was neglected and only the absolute amplitudes are presented in the table. Because the PatLoc SEM coil is physically rotated, both channels are comprised of both terms, A22 and B22. The individual magnitudes of the spherical harmonics correspond to the rotational symmetry of the two PatLoc SEM channels. The amplitudes of the individual components geometrically combined are also listed in the table to give a better idea of the SEM composition for each order. The rotation angle demonstrates the offset to the second order shim to geometrically decouple the PatLoc SEM coil, and also demonstrates the rotational offset of 45° between both PatLoc SEMs. The PatLoc SEM

coil was not industrially manufactured explaining the misalignment of 3% of the two SEMs with respect to each other.

Simulated Encoding Fields

Table 2 shows the amplitudes of the spherical harmonics for the simulated PatLoc SEM. All relevant components are given for the inner PatLoc 1 SEM, as the amplitudes of these components vary only within 0.5% for the PatLoc 2. The main components of the concomitant field components are linear, with some ZX- and ZY- components which are quadratic saddle fields but with different orientation. All other or higher order components contribute with less than 1% and are also disregarded.

Transverse Magnetic Fields

Figure 6 compares the measured fieldmap of the transverse component B_t of the magnetic encoding field against simulated data. Simulated B_x and B_y were used to calculate B_t, based on Eq. (4). The measured data were corrected for a field offset based on reference measurements in a box of 25 × 5 voxels along the main axis of the PatLoc SEM coil, where the phase is expected to be zero

Table 2 Spherical Harmonic Constituents of the Simulated PatLoc 1 Field, in % of the Maximum Field Inside the Analyzed Sphere

Spherical Harmonic	Analytical Expression	B_x (%)	B_y (%)	B_z (%)
A11	X	$\mathbf{91.2 \pm 4.4}$	<0.01	<0.01
B11	Y	<0.01	$\mathbf{91.2 \pm 4.4}$	<0.01
A21	ZX	$\mathbf{25.2 \pm 5.5}$	<0.01	<0.01
B21	ZY	<0.01	$\mathbf{25.2 \pm 5.5}$	<0.01
A22	$X^2 - Y^2$	<0.01	<0.01	$\mathbf{98.7 \pm 22.3}$
B22	$2XY$	<0.01	<0.01	<0.01
A20	$Z^2 - (X^2 + Y^2)/2$	<0.01	<0.01	<0.01
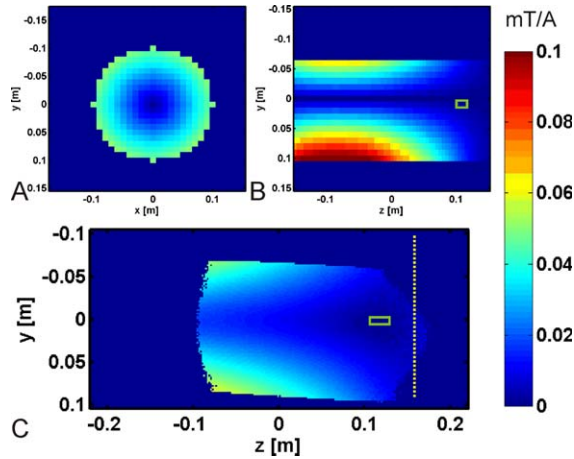
Figure 6 Top row simulated transverse component of the PatLoc 1 channel, all subfigures are in mT/A. (A) A transverse cut through the magnet and PatLoc isocenter and in (B) a coronal slice. (C) The measured Br of the PatLoc SEM 1, where the imaged slice is rotated to match the simulated data. The green box indicates the region which is used for data correction in B and C and the yellow dotted line in C visualizes the edge of the SEM coil.

[confirmed through simulated data, green box in Figs. 6(B,C)], to yield correct values for B_t^2.

Figure 6 shows 2D fieldmaps of the simulated and measured transverse component of the encoding field at the isocenter and the measured coronal slice. The data of the transverse field measurement were analyzed in a 1D representation at the isocenter and at positions $z = \pm 50$ mm from the isocenter [Fig. 7(A)]. The transverse component B_t increases

Table 3 Amplitude and Time Constant of the Measured Eddy Currents of the PatLoc SEM Coil

	Amplitude (%)	Time Constant (ms)
PatLoc 1	1.01 ± 0.01	422 ± 12
PatLoc 2	1.17 ± 0.02	418 ± 16

These Values Are Used for Eddy Current Compensation.

toward the service end of the coil containing tightly packed return paths (negative z-direction), where more wires are contributing to B_t than B_z. The largest discrepancy between measured data and simulated data were 4%, normalized to the maximum of the simulated transverse component B_t within a 200 mm sphere.

The variation along the z-direction at $x = 0$ mm, $y = 50$ mm is depicted in Fig. 7(B), where it is also compared with simulated data. In the figure, it can be seen clearly that the transverse component of the magnetic field drops quickly toward zero at the patient end and increases toward the service end of the coil.

Eddy Current Performance

The measured eddy currents for both PatLoc SEMs are $1 \pm 0.2\%$ with time constants of 410 ± 10 ms, with the PatLoc 2 SEM exhibiting slightly stronger eddy currents, see Table 3. Figure 8 shows fieldmaps for the first time point of TE = 4.8 ms, where the eddy currents are the strongest. Using the obtained compensation values, the amplitude of the eddy currents can be significantly reduced from 1% to
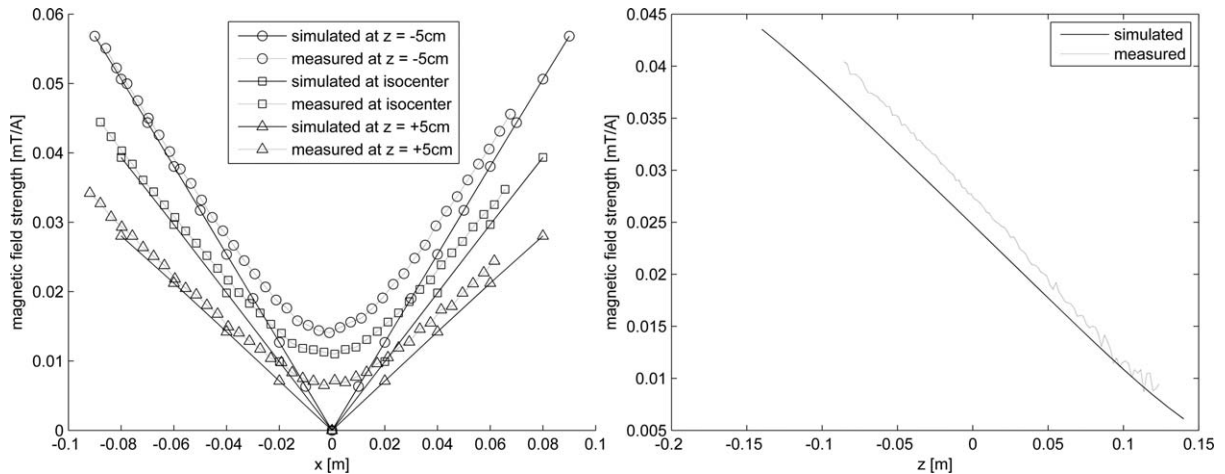
Figure 7 Comparison of calculated and measured transverse component of the field B_t in mT/A which leads to the concomitant field term. (A) A 1D representations along the transverse slice at the isocenter and $z \pm 50$ mm. The solid line plots the simulated data and the dotted the measured and corrected data in both plots. (B) A 1D representation along the z-direction of the measured coronal slice at $y = 50$ mm.
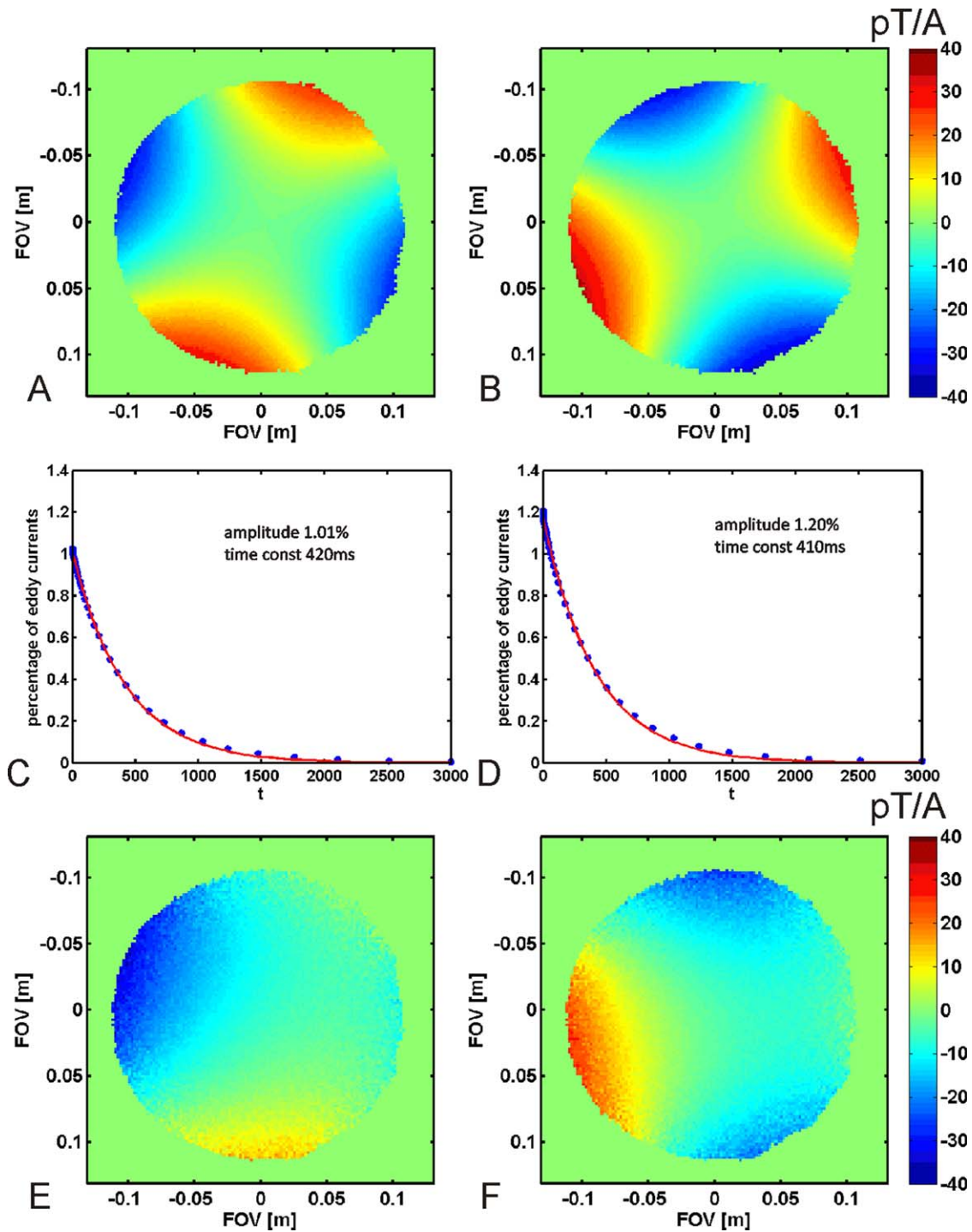
Figure 8   The eddy current fieldmaps are in pT/A ahown here the first measurement point of 4.8 ms after the PatLoc pulse. (A) and (B) The measured fieldmaps of the eddy currents without correction for PatLoc channel 1 and 2, respectively. (C) and (D) The amplitudes of the eddy current decays fitted with an exponential function as described. (E) and (F) The residual eddy current maps after correction.

0.04%. With this present experimental setup, only the self-eddy currents can be corrected together with the cross terms between the PatLoc SEM channels. The hardware architecture of the scanner does not currently allow compensation for cross terms between the PatLoc-induced eddy currents and the linear SEMs. This is not expected to be an issue, however, as eddy current levels of 0.04% can be considered negligible for most MR experiments.

In analyzing the data with the negative SEM lobe, the amplitude and timing parameters show that the eddy current behaviour is symmetric with respect to the sign of the provoking SEM lobe.

Human Images

The images depicted in Figs. 9(A,B) show the acquisition with the linear gradients, and C and D the PatLoc acquisitions reconstructed with a CG-method (3). Both images were acquired using the same acquisition parameters. The resolution of the PatLoc acquisition is higher at the periphery while exhibiting the typical loss of resolution toward the middle of the acquired image where the quadratic SEMs are flat and provide no encoding. In addition, a residual star-like Gibbs ringing artefact is visible in the final reconstructed PatLoc image. The image acquired with linear gradients has a resolution of 0.9 mm/pixel and the PatLoc image has 0.3 mm/pixel at the periphery of the brain (the resolution for a PatLoc image is not constant across the FOV, (2)). No PNS or other unpleasant sensations were reported by the volunteer in this experiment.

DISCUSSION

A PatLoc SEM coil using non-linear magnetic fields for signal encoding was successfully developed, built and integrated into an MR scanner. Presented in this article are the detailed steps which led us from the conception through the implementation and toward the comprehensive characterization of this coil. It is noteworthy that, although the main intention in building this coil was to enable a number of proof-of-concept PatLoc experiments (2,3,6–9,31), it has also proven to perform beyond the initial expectations with respect to eddy-current performance and the presence of the PatLoc SEM coil within the magnet has a negligible influence on the performance of the standard linear gradients.

Most gradient and shim coils are designed using the target field method (32). This involves using the spherical harmonics as a basis and minimizing all unwanted residual terms. A streamline of the cur-
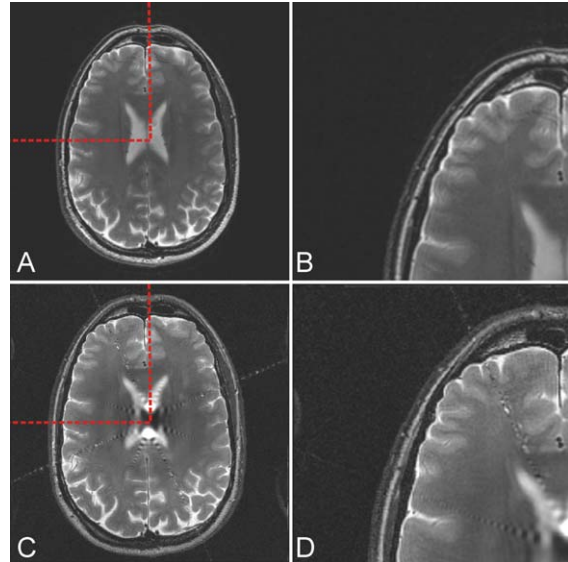
Figure 9   (A) The reference image acquired with linear gradients. (B) zoom of A). (C) The PatLoc image of the same slice as in A. (D) zoom of C. Demonstrating increased resolution at periphery. The red dotted lines visualize the zoomed regions from B and D.

rent generating this target magnetic field is obtained and discretised into a gradient coil design (33–35). If the final shape of the PatLoc SEM coil is given by other design constraints, the GSA (19) is also a valid method, as used in this article. Based on a simple design from Cho and Yi (36), our PatLoc SEM coil elements were modified to an asymmetric basic layout. The basic layout was further optimized to generate the desired PatLoc SEMs using GSA optimization. This method yields good results if a reasonable basic SEM coil shape is given as the initial design value and then optimized to the desired target magnetic field. For a higher specification PatLoc SEM coil, which can be driven with higher currents up to 600A, a symmetric layout and streamline method was applied (37). The sensitivity of this industrially manufactured PatLoc SEM coil is 1.38 and 1.57 $mT/m^2/A$ compared with 1.34 and 1.44 $mT/m^2/A$. The presented GSA method has also been successfully applied to design a monoplanar SEM system for body imaging with non-linear SEMs (38).

Eddy currents of the linear gradients for a normal MRI scanner are characterised by the manufacturer and the preemphasis terms typically only need to be updated when the gradients or other paramagnetic or ferrous components influencing the electromagnetic properties of the scanner are changed. However, this might not perfectly compensate for eddy currents and might require further adjustments using a different method (39,40). For the special

scanner setup, with six available gradient channels, it is possible to use the linear gradients to visualise in 2D or even 3D (in contrast to some of the previous methods where FIDs are measured (40,41)) the eddy currents induced by switching the additional SEMs. The eddy currents for this PatLoc SEM coil are small (1%) despite the fact that the PatLoc SEM coil is unshielded. The quadrupolar geometry of the SEMs is beneficial as the magnetic field outside of the PatLoc SEM coil decays more rapidly compared to conventional linear fields (1/r5 instead of 1/r3) leaving only small residual fields at the eddy current carrying surfaces within the bore of the MRI scanner. At 1%, the eddy currents are small enough such that they could be neglected in previous measurements using the same hardware (3,6–9,31). However, as demonstrated here, the main component can be well corrected for. For example, it has been shown that multi-dimensional encoding schemes such as 4D-RIO (9) or O-space imaging trajectories (30) require a very high accuracy of the effective encoding fields to avoid artefacts in the reconstructed images. Remaining magnetic field residuals, due to multiple eddy current components with different time-constants, as well as cross terms, have been neglected as their effect can be considered negligible.

The transverse field was measured and evaluated with respect to simulated data to demonstrate the viability of the simulated data for estimating PNS for safe operation in the first controlled mode. A preliminary experimental measurement with a pickup coil gave comparable results (15). With all return paths positioned at the service end of the coil, the transverse component of the fields reduces quickly to zero in the shoulder region of the volunteer and is therefore demonstrated to be largely irrelevant for PNS-performance. The difference in field strength at the same distance above and below isocenter probably reflects a slight asymmetry of the PatLoc SEM coil due to the manufacturing tolerances. The discrepancy of 4% between measured and simulated data indicate that the PatLoc SEM coil was not perfectly aligned along the z-direction and not perfectly positioned relative to the isocenter. However, as the larger B_t fields are toward the service end of the PatLoc SEM coil, which the volunteer does not reach, the discrepancy of the measured and simulated data are irrelevant for assessment of PNS. The concomitant fields for this special geometry vary approximately linearly in r and z and are large enough to be non-negligible compared to the imaging gradient B_z causing additional dephasing, especially for long single shot trajectories (5,6,9,42).

Initial PatLoc imaging experiments ensured that the limit of 20T/s was not exceeded. Later experiments, especially when combining the PatLoc SEMs with linear SEMs included a stepwise increase of all SEM amplitudes up to the desired SEM amplitude (3,6,7,29). With the volunteer experiments presented here, using only the PatLoc SEMs for imaging, no PNS was reported although the PatLoc SEM coil was driven at the limits of the specifications. In part this is because this prototype PatLoc SEM coil is limited to a relatively low current and correspondingly to relatively low maximum induced fields. In addition, insert coils are known to produce more local fields with a smaller potential of introducing PNS than whole-body gradient systems. It is therefore neither sensible nor feasible to directly compare PNS performance of the available hardware.

The star shaped artefact is visible in the PatLoc images, both in phantom and *in vivo*. With the particular SEM geometry signal from the center region of the object, where encoding fields are flat, is not dephased even at the k-space periphery, resulting in a Gibbs-ringing artefact with eight spokes. In phantom imaging this artefact can efficiently be filtered, in *in vivo* images however it cannot be fully suppressed (3) possibly due to motion of the volunteer. This artefact is known to only occur with cartesian trajectories and not with radial PatLoc imaging (3).

CONCLUSION

In conclusion, the design and the construction of a head SEM insert for PatLoc imaging was described and its performance characterized. The coil has proven to be reliable and suitable for proof-of-concept *in vivo* experiments. PNS behavior of the coil could be assessed using a combination of measured data and simulations. Due to the asymmetric coil design, the transverse field components decay rapidly toward the subject's shoulders and thus are largely irrelevant for PNS performance. Eddy currents of this non-shielded coil have been well characterised and corrected for.

ACKNOWLEDGMENTS

Stark's help in tuning and matching the RF shield are acknowledged.

REFERENCES

1. Hennig J, Welz AM, Schultz G, Korvink J, Liu Z, Speck O, Zaitsev M. 2008. Parallel imaging in non-bijective, curvilinear magnetic field gradients: a concept study. MAGMA 21:5–14.

2. Schultz G, Ullmann P, Lehr H, Welz AM, Hennig J, Zaitsev M. 2010. Reconstruction of MRI data encoded with arbitrarily shaped, curvilinear, nonbijective magnetic fields. Magn Reson Med 64:1390–1403.

3. Schultz G, Weber H, Gallichan D, Witschey WRT, Welz AM, Cocosco CA, Hennig J, Zaitsev M. 2011. Radial imaging with multipolar magnetic encoding fields. IEEE Trans Med Imaging 30:2134–2145.

4. Schultz G. 2013. Magnetic Resonance Imaging with Nonlinear Gradient Fields—Signal Encoding and Image Reconstruction. Springer Spektrum, Springer Fachmedien Wiesbaden, Germany.

5. Gallichan D, Testud F, Barmet C, Cocosco CA, Welz AM, Pruessmann KP, Hennig J, Zaitsev M. 2012. Simultaneous linear and nonlinear encoding in a single shot. In Proceedings of the 20th Scientific Meeting and Exhibition of ISMRM. Melbourne. 292 p.

6. Layton KJ, Gallichan D, Testud F, Cocosco CA, Welz AM, Barmet C, Pruessmann KP, Hennig J, Zaitsev M. Single shot trajectory design for region-specific imaging using linear and nonlinear magnetic encoding fields. Magn Reson Med, DOI: 10.1002/mrm.24494.

7. Witschey WRT, Cocosco CA, Gallichan D, Schultz G, Weber H, Welz A, Hennig J, Zaitsev M. 2012. Localization by nonlinear phase preparation and k-space trajectory design. Magn Reson Med 67:1620–1632.

8. Weber H, Gallichan D, Schultz G, Cocosco CA, Littin S, Reichardt W, Welz A, Witschey W, Hennig J, Zaitsev M. 2013. Excitation and geometrically matched local encoding of curved slices. Magn Reson Med 69:1317–1325.

9. Gallichan D, Cocosco CA, Dewdney A, Schultz G, Welz A, Hennig J, Zaitsev M. 2011. Simultaneously driven linear and nonlinear spatial encoding fields in MRI. Magn Reson Med 65:702–714.

10. Lin F-H, Witzel T, Schultz G, Gallichan D, Kuo W-J, Wang F-N, Hennig J, Zaitsev M, Belliveau JW. 2012. Reconstruction of MRI data encoded by multiple nonbijective curvilinear magnetic fields. Magn Reson Med 68:1145–1156.

11. Bernstein MA, Zhou XJ, Polzin JA, King KF, Ganin A, Pelc NJ, Glover GH. 1998. Concomitant gradient terms in phase contrast MR: analysis and correction Magn Reson Med 39:300–308.

12. Badea EA, Craiu O. 1997. Eddy current effects in MRI superconducting magnets. IEEE Trans Magn 33:1330–1333.

13. Norris DG, Hutchison JMS. 1990. Concomitant magnetic field gradients and their effects on imaging at low magnetic field strengths. Magn Reson Med 8:33–37.

14. Irnich W, Schmitt F. 1995. Magnetostimulation in MRI. Magn Reson Med 33:619–623.

15. Cocosco CA, Dewdney A, Dietz P, Semmler M, Welz AM, Gallichan D, Weber H, Schultz G, Hennig J, Zaitsev M. 2010. Safety considerations for a PatLoc gradient insert coil for human head imaging. In Proceedings of the 18th Scientific Meeting and Exhibition of ISMRM. Stockholm. 3946 p.

16. Welz AM, Zaitsev M, Cocosco CA, Weber H, Jia F, Liu Z, Schmidt H, Lehr H, Post H, Dewdney A, Hennig J. 2009. Development of a non-shielded PatLoc gradient insert for human head imaging. In Proceedings of the 17th Scientific Meeting and Exhibition of ISMRM. Honolulu. 3073 p.

17. Poole M, Bowtell R. 2007. Novel gradient coils designed using a boundary element method. Concepts Magn Reson B: Magn Reson Eng 31B:162–175.

18. Liu Z, Jia F, Zaitsev M, Welz AM, Schultz G, Korvink JG, Hennig J. 2008. Parametrical optimization of a PatLoc gradient coil. In Proceedings of the 16th Scientific Meeting and Exhibition of ISMRM. Toronto. 1164 p.

19. Dorn W, Gomory R, Greenberg H. 1964. Automatic design of optimal structures. J Mec 1964, 3:25–52.

20. Jia F. 2010. Design Optimization of MRI Gradient Coils. PhD thesis. Universität Freiburg.

21. Fontius U, Baumgartl R, Boettcher U, Doerfler G, Hebrank, Fischer D, Jeschke H, Kannengießer S, Kwapil G, Nerreter U, Nistler J, Pirkl G, Potthast A, Roell S, Schor S, Stoeckel B, Adelsteinson E, Gregor A, Alagappan V, Gagoski B, Setsompop K, Wald L, Schmitt F. 2006. A Flexible 8-Channel RF Transmit Array System for Parallel Excitation. In Proceedings of the 14th Scientific Meeting and Exhibition of ISMRM. Seattle. 127 p.

22. Shenberg I, Macovski A. 1985. Inhomogeneity and multiple dimension considerations in magnetic resonance imaging with time-varying gradients. IEEE Trans Med Imaging 4:165–174.

23. Noll DC, Meyer CH, Pauly JM, Nishimura DG, Macovski A. 1991. A homogeneity correction method for magnetic resonance imaging with time-varying gradients. IEEE Trans Med Imaging 10:629–637.

24. DuMouchel WH, O'Brian FL. 1989. Integrating a robust option into a multiple regression computing environment. In Computer Science and Statistics: Proceedings of the 21st Symposium on the Interface. Alexandria, VA.

25. Hillenbrand DF, Lo KM, Punchard WFB, Reese TG, Starewicz PM. 2005. High-order MR shimming: a simulation study of the effectiveness of competing

methods, using an established susceptibility model of the human head. Appl Magn Reson, 29:39–64.

26. Romeo F, Hoult DI 1984. Magnet field profiling: analysis and correcting coil design. Magn Reson Med 1:44–65.

27. Testud F, Zaitsev M. 2009. B0 field monitoring by air-matched phantoms. In Proceedings of the 17th Scientific Meeting and Exhibition of ISMRM. Honolulu. 2791 p.

28. Cocosco CA, Gallichan D, Dewdney AJ, Schultz G, Welz AM, Witschey WRT, Weber H, Hennig J, Zaitsev M. 2011. First In-vivo Results with a PatLoc Gradient Insert Coil for Human Head Imaging. In Proceedings of the 19th Scientific Meeting and Exhibition of ISMRM. Montreal. 714 p.

29. Gallichan D, Cocosco CA, Schultz G, Weber H, Welz AM, Hennig J, Zaitsev M. 2012. Practical considerations for in vivo MRI with higher dimensional spatial encoding. MAGMA 25:419–431.

30. Stockmann JP, Ciris PA, Galiana G, Tam L, Constable RT. 2010. O-space imaging: highly efficient parallel imaging using second-order nonlinear fields as encoding gradients with no phase encoding. Magn Reson Med 64:447–456.

31. Witschey WRT, Littin S, Cocosco CA, Gallichan D, Schultz G, Weber H, Welz A, Hennig J, Zaitsev M. 2013. Stages: sub-Fourier dynamic shim updating using nonlinear magnetic field phase preparation. Magn Reson Med, DOI: 10.1002/mrm.24494.

32. Turner R. 1986. A target field approach to optimal coil design. J Phys D: Appl Phys 19:L147–L151.

33. Brideson MA, Forbes LK, Crozier S. 2002. Determining complicated winding patterns for shim coils using stream functions and the target-field method. Concepts Magn Reson 14:9–18.

34. Forbes LK, Crozier S. 2001. A novel target-field method for finite-length magnetic resonance shim coils: I. Zonal shims. J Phys D: Appl Phys 34:3447–3455.

35. Bowtell R, Robyr P. 1998. Multilayer gradient coil design. J Magn Reson 131:286–294.

36. Cho Z, Yi J. 1991. A novel type of surface gradient coil (1969). J Magn Reson 94:471–485.

37. Zaitsev M, Punchard W, Dewdney A, Gallichan D, Stockman J, Cocosco CA, Littin S, Welz AM, Weber H, Starewicz P, Hennig J. 2012. Design and Implementation of High-Performance Non-Linear PatLoc Gradient Coil. In Proceedings of the 20th Scientific Meeting and Exhibition of ISMRM. Melbourne. 2591 p.

38. Littin S, Gallichan D, Welz AM, Dewdney A, Jia F, Cocosco CA, Hennig J, Zaitsev M. 2012. Monoplanar gradient system for imaging with nonlinear gradients. In Proceedings of the 20th Scientific Meeting and Exhibition of ISMRM. Melbourne. 698 p.

39. Reese TG, Heid O, Weisskoff RM, Wedeen VJ. 2003. Reduction of eddy-current-induced distortion in diffusion MRI using a twice-refocused spin echo. Magn Reson Med 49:177–182.

40. Terpstra M, Andersen PM, Gruetter R. 1998. Localized eddy current compensation using quantitative field mapping. J Magn Reson 131:139–143.

41. Jehenson P, Westphal M, Schuff N. 1990. Analytical method for the compensation of eddy-current effects induced by pulsed magnetic field gradients in NMR systems (1969). J Magn Reson 90:264–278.

42. Testud F, Gallichan D, Layton KJ, Welz AM, Barmet C, Cocosco CA, Pruessmann KP, Hennig J, Zaitsev M. 2013. Single Shot Multi-Dimensional Imaging using Magnetic Field Monitoring and including Maxwell Terms. In Proceedings of the 21th Scientific Meeting and Exhibition of ISMRM. Salt Lake City. 2663 p.